

Near-Infrared Synchrotron Emission from Cas A

Jeonghee Rho

*SIRTF Science Center, California Institute of Technology, MS 220-6, Pasadena, CA 91125;
e-mail: rho@ipac.caltech.edu*

Stephen P. Reynolds¹

Harvard-Smithsonian Center for Astrophysics, 60 Garden St., Cambridge, MA 02138

William T. Reach, Tom H. Jarrett

SIRTF Science Center/IPAC, California Institute of Technology, MS 220-6, Pasadena, CA 91125

Glenn E. Allen

MIT Center for Space Research, 77 Massachusetts Avenue, NE 80-6029, MA 02139-4307

John C. Wilson²

Space Sciences Building, Cornell University, Ithaca, NY 14853

ABSTRACT

Recent high energy observations of Cas A suggests the presence of synchrotron radiation, implying acceleration of cosmic rays by young supernova remnants. We detect synchrotron emission from Cas A in the near-infrared using Two Micron All Sky Survey (2MASS) and Palomar 200 inch PFIRCAM observations. The remnant is detected in J, H, and K_s bands using 2MASS: K_s band is the brightest, H is moderate and J is faint. In the J and H bands, bright [Fe II] lines (1.24 μ m and 1.64 μ m) are detected spectroscopically. The Palomar observations include K_s continuum, narrow-band 1.64 μ m (centered on [Fe II]) and 2.12 μ m (centered on H₂(1-0)) images. While the narrow-band 1.64 μ m image shows filamentary and knotty structures, similar to the optical image, the K_s image shows a relatively smooth, diffuse shell, remarkably similar to the radio image. The H₂ image is identical to the K_s continuum image with surface brightness reduced as expected for the ratio of filter bandwidths, showing no contribution of H₂ lines to the K_s-band image. The broad-band near-infrared fluxes of Cas A are generally consistent with, but a few tens of percent higher than, an extrapolation of the radio fluxes. The hardening to higher frequencies is possibly due to nonlinear shock acceleration and/or spectral index variation across the remnant. We show evidence of spectral index variation across Cas A using the ‘spectral tomography’ technique. The presence of near-infrared synchrotron radiation requires the roll-off frequency to be higher than 1.5×10^{14} Hz, implying that electrons are accelerated to

energies of at least $E = 0.3B_{\text{mG}}^{-1/2}$ erg or 0.2 TeV. The morphological similarity in diffuse emission between the radio and K_s band images implies that synchrotron losses are not dominant, or we would expect to see a greater concentration in knots. We also show dust continuum is not significant in the near-infrared emission of Cas A. Our observations show unambiguous evidence that the near-infrared K_s band emission of Cas A is from synchrotron emission by accelerated cosmic-ray electrons.

Subject headings: Supernova remnants: Cas A – Near-infrared – Particle acceleration

1. Introduction

The origin of cosmic rays has been unclear since their discovery (Elster et al. 1969). It has been widely thought that their energy is derived from supernovae, which are naturally associated with particle acceleration because they are the primary energy input for interstellar gas. Shocks are thought to be primary acceleration sites of cosmic rays. Some evidence that cosmic-ray electrons are accelerated in supernova remnant shocks has been recently found using X-ray and gamma-ray observations. SN 1006 is a notable example. Its X-ray emission shows featureless spectra in the limb, strong evidence that the emission is synchrotron radiation (Koyama et al. 1995). The detection of TeV gamma-rays, probably cosmic-ray background photons upscattered by ~ 100 TeV electrons, strengthened the claim of synchrotron emission in SN 1006 (Tanimori et al. 1998). There are a few other SNRs including G347.3-05 (Koyama et al. 1997; Slane et al. 1999), and G266.2-1.2 (Slane et al. 2001), which show featureless X-ray spectra, possibly due to synchrotron emission. Other examples of synchrotron emission are less clear, complicated by mixture with thermal emission, such as Cas A and RCW 86 (Allen et al. 1997; Borkowski et al. 2000; Rho et al. 2002).

However, even if synchrotron radiation commonly contributes to the X-ray emission of SNRs, it does so at a level below the extrapolation from radio frequencies, by factors of 3 to 100 for 14 Galactic SNRs (Reynolds & Keohane 1999) and 11 SNRs in the LMC (Hendrick & Reynolds 2001). That is, the electron distribution responsible for radio synchrotron emission must steepen at energies below 100 TeV in all those 25 cases. This is problematic if SNRs are to accelerate cosmic rays up to the slight steepening around 3000 TeV in the cosmic ray ion spectrum known as the ‘knee.’ While relativistic electrons may be subject to radiative losses during the acceleration process, this should not be a problem for ions, so perhaps in all those cases electron acceleration is limited by losses, while ion acceleration invisibly extends to much higher energies. Alternatively only certain remnants (for instance, much older and larger ones than in the Reynolds & Keohane (1999) study) may produce the highest energy cosmic rays. Another possibility is that a few remnants, such as Cas A, have very much stronger magnetic fields, increasing both the acceleration

¹Permanent address: Department of Physics, North Carolina State University, Raleigh, NC 27695

²Present Address: 255 Astronomy Bldg, University of Virginia, 530 McCormick Rd, Charlottesville, VA 22903.

rate and the importance of losses so that the required steepening in the electron spectrum can be due to losses while ion acceleration can extend to 10^{15} eV and beyond (Ellison et al. 1999). Perhaps Cas A is a ‘super-accelerator’ of cosmic rays.

While the observed X-rays from Cas A fall below the radio extrapolation by a smaller factor than any other Galactic SNR in the Reynolds & Keohane sample, this of course does not demonstrate that a portion of those X-rays are due to synchrotron emission. Most of soft X-rays (below 7 keV) are clearly thermal (e.g., Gotthelf et al. 2001) but emission is seen up to energies > 10 keV (Allen et al. 1997) with the *Rossi X-ray Timing Explorer* (RXTE), and to ~ 100 keV with OSSE on the *Gamma Ray Observatory* (The et al. 1996). The latter study shows a power-law photon index of -3.1 ± 0.4 . A spectrum this hard to such high energies cannot be produced by synchrotron emission from shock-accelerated electrons in any reasonable model. The most likely explanation is nonthermal bremsstrahlung (NTB) (see, for instance, Asvarov et al. 1989; Laming 2001) from the lowest-energy nonthermal electron population, the beginning of the distribution that extends up to radio-emitting electrons at around 1 – 10 GeV. Evidence for at least some X-ray synchrotron emission near shock fronts was reported by Gotthelf et al. (2001), but the total emission in the apparent synchrotron component is a small fraction of the total flux in the 4 – 6 keV range, and Bleeker et al. (2001) cite observations from *XMM-Newton* to assert only a small role for synchrotron emission in the total X-ray flux. Thus the question of the highest frequency at which Cas A shows unambiguous synchrotron emission remains open.

Recently, a 5σ detection of Cas A has been reported at γ -ray energies above 1 TeV with the HEGRA Stereoscopic Čerenkov Telescope System (Aharonian et al. 2001). The emission could be due to leptonic processes (NTB or inverse-Compton upscattering of cosmic microwave background photons) or hadronic (inelastic cosmic-ray proton collisions with ambient gas producing neutral pions which decay to gamma-rays). NTB would require electrons of energies of a few TeV; π^0 -decay gamma rays would require similar energies for protons. Inverse-Compton emission from the cosmic microwave background, however, would indicate the presence of electrons of energies of order 100 TeV. However, until this detection is confirmed and the nature of the processes producing the gamma rays clarified, the highest particle energies present in Cas A are still uncertain.

The EGRET limits on emission above 100 MeV (Esposito et al. 1996) can be used to put a lower limit on the magnetic-field strength of at least 0.4 mG (Atoyan et al. 2000); if the field were weaker, the required relativistic electron density would have to be higher to explain the radio emission, and those electrons would emit NTB at levels higher than the upper limit in the EGRET band. Thus Cas A seems to have a much larger magnetic field than inferred for other remnants (e.g., $\sim 10 \mu\text{G}$ for SN 1006; Tanimori et al. 1998, Dyer et al. 2001).

The total flux of Cas A at millimeter wavelengths (Liszt & Lucas 1999; Mezger et al. 1986) lies very close to the extrapolation from centimeter wavelengths. Shortward of 1.2 mm, however, there is very little information. Synchrotron continuum is required to fit the mid-infrared ISOCAM and ISO-SWS (6-30 μm) spectra and the spectral shape of synchrotron emission (i.e. power law)

dominates between 6–8 μm (Douvion, Lagage, & Pantin 2001). Tuffs et al. (1997) suspected from ISO data that emission in a line-free region near 6 μm could be synchrotron. Gerardy & Fesen (2001) report that a K-band image resembles the radio, but gave no quantitative flux determinations. Here we search for synchrotron emission from Cas A in the infrared, and show a definitive detection of synchrotron radiation at near-infrared wavelengths. We discuss the implications of our result for theories of particle acceleration and cosmic-ray origin in supernova remnants.

2. Observations and Results

2.1. 2MASS

The 2MASS images of Cas A were obtained as part of the routine observations for the Two Micron All Sky Survey (2MASS; Skrutskie et al. 1997; Cutri et al. 2002) using the northern telescope at Mt. Hopkins, Arizona, on 1998 December 26. The wavelength coverages of the bands are 1.11-1.36 μm (J), 1.5-1.8 μm (H) and 2-2.32 μm (K_s). The spatial resolution of 2MASS is 3". The detailed calibration of diffuse emission is explained in Rho et al. (2001). Here we used updated zero-point fluxes of 1592, 1024, and 668.8 Jy for J, H, and K_s , respectively. Figure 1 shows the 2MASS three-color image of Cas A, revealing a shell-like morphology for the near-infrared emission. The K_s and H band images are brighter than the J band image, and the J band emission is barely detected in 2MASS. The differences in morphology among the three bands are not very noticeable except in the southwestern shell. The three color image in Figure 1 contrasts the difference: K_s emission (reddish in color) dominates for most of Cas A, and H band emission (greenish in color) is more noticeable in the southwestern shell, some inner part of the northern shell, and sparsely distributed knots.

We obtained a few near-infrared spectra of Cas A using the CorMASS instrument (Wilson et al. 2001) on the Palomar 60" telescope. The observations took place on Sep. 10-12 and Nov. 14-15, 2000. The CorMASS spectra towards the northwestern and southwestern shell show bright lines of [Fe II] in the J and H bands (at 1.26 μm and 1.64 μm), which is consistent with the spectra of Gerardy & Fesen (2001), and no lines in the K_s band were detected. We also took the spectra towards possibly synchrotron dominated positions (positions D and C in Hughes et al. (2000) where no or weak X-ray emission lines are detected), and [Fe II] was not detected. This indicates the line emitting region is spatially limited across the remnant. The line contribution to each filter is estimated based on the near-infrared spectra from Gerardy & Fesen (2001), which is described in the next section.

2.2. Palomar 200 inch PFIRCAM images

We observed Cas A on July 12–13, 2001 using the Prime Focus Infrared Camera (PFIRCAM) on the Hale 200-inch telescope on Palomar Mountain. The PFIRCAM has a 256×256 pixel array, with a pixel scale of $0.494''$ at the $f/3.3$ prime focus of the 200-inch telescope. We took K_s broad band ($\Delta\lambda = 0.32\mu\text{m}$), [Fe II] narrow filter ($\lambda = 1.64\mu\text{m}$; $\Delta\lambda = 0.016\mu\text{m}$) and H_2 ($\lambda = 2.12\mu\text{m}$, $\Delta\lambda = 0.02\mu\text{m}$) images. Our goal was to distinguish the structures between the line and continuum as well as to measure the remnant fluxes. The seeing was $1''$ to $1.5''$. We used the observational technique described in Reach et al. (2002).

The integration times per sky pixel for the K_s , Fe II, and H_2 images are 30, 60, and 60 sec, respectively. The PFIRCAM images were calibrated by comparing photometry of sources in the field to the 2MASS catalog (Cutri et al. 2002). The K_s image was calibrated using 68 stars with 2MASS K_s magnitudes ranging from 12.5 to 14.5, the H_2 -band image was calibrated using 43 stars with 2MASS K_s magnitudes ranging from 11.0 to 14.5, and the [Fe II] image was calibrated using 52 stars with 2MASS H-band magnitudes ranging from 12.6 to 14.6. Bright stars were excluded from the fit because of non-linearity in the PFIRCAM data; the diffuse emission is equivalent to stars fainter than 18^{th} magnitude and is well within the linear regime of the detector. The total remnant fluxes were measured from the near-infrared images after subtracting stars using the DAOPHOT package. The regions ($9''$ radius) of two bright stars in the west were excluded from the estimation of the total fluxes.

The narrow-band mosaiced image of [Fe II] in Figure 2 (in blue) is globally similar to the optical image (Douvion, Lagage, & Pantin 2001; Fesen, Becker & Blair 1987), showing sharp filamentary and knotty structures of Fe-rich ejecta. However, while [Ne] and [S II] optical maps show brighter emission in the north, the [Fe II] image shows much brighter emission in the southwest.

Figures 2 (in red) and 3a show the Palomar PFIRCAM K_s band image, which is noticeably different from the Fe II-band image. The K_s -band structure is much smoother than the ejecta structure that dominates the [Fe II] and optical images. The H_2 -band image is essentially identical to the K_s image, with surface brightness reduced (and noise increased) as expected for the ratio of filter bandwidths; thus the H_2 band appears to be completely due to the same continuum that generates the the K_s -band image. We show the 1.4 GHz radio image (Anderson et al. 1991) in Figure 3b for comparison with the K_s band image, because they are remarkably similar. The radio image of (Anderson et al. 1991) has a pixel size of $0.4''$ and a spatial resolution of $1.3''$, which is comparable to our Palomar image. The similarity between the K_s band and radio images suggests that both the K_s and radio images are due to the same physical process: synchrotron radiation.

3. Infrared Flux of Cas A

3.1. Total flux from near-infrared images

The total remnant flux from the PFIRCAM K_s band image is 0.32 ± 0.03 Jy, where the error includes the uncertainty in calibration. In comparison, the 2MASS flux in the K_s band is 0.31 ± 0.02 Jy. Although the 2MASS diffuse emission may include some faint stars due to lower spatial resolution, the K_s band flux is consistent between PFIRCAM and 2MASS. The statistical errors of the measurement are less than 1%, but a larger error is induced by the method of star subtraction because sometimes the sampling of the fluxes for the stars is insufficient or it is unclear if the bright blobs are faint stars or diffuse emission, especially in the [Fe II] image. We experimented with different thresholds of star identification, and we believe the error would not be larger than 20% of the measured flux (a conservative estimate). Extinction varies across the remnant, with A_v ranging typically from 4.3 to 6.2 mag (Searle 1971; Fesen, Becker & Blair 1987), and as high as 8 mag in the western boundary (Hurford & Fesen 1996). The extinction-corrected K_s flux is $0.53^{+0.12}_{-0.04}$ Jy, using the near-infrared extinction law of Rieke & Lebofsky (1985); the error includes the possible range of extinction. The CorMASS spectra show no lines in the K_s band, and Gerardy & Fesen (2001) also detected no lines within the K_s band (2–2.3 μm) from FMK (fast moving knot) positions in the north and northeast of the remnant, while they detected faint lines of [Fe II], He I, and H II Br γ from QSF (quasi-stationary flocculi) positions in the southwest. It is likely the line contribution is very small in the K_s band image, considering that (1) QSF covers a small portion of the remnant, (2) the morphology of the K_s image is remarkably similar to the radio image, and (3) the narrow filter 2.12 μm image is very similar to the K_s -band image.

The total flux of the PFIRCAM [Fe II] image is 0.37 ± 0.06 Jy, and the extinction-corrected flux is 0.76 Jy using A_v of 4.5 mag. This total flux is somewhat uncertain, because the [Fe II] emission is knotty and filamentary and some of the bright peaks of diffuse emission may have been subtracted during subtraction of stars. The 2MASS total flux in the H band is 0.27 Jy, and the extinction-corrected flux is 0.56 Jy. The 2MASS H band flux may be somewhat overestimated due to contribution from unresolved faint stars. Experimenting with different star-subtraction methods shows that neither of these effects is significant.

Emission lines contribute a small fraction of the flux observed in the wide K_s band. We estimate the line contribution as follows. We assume that the the emission in each band arises from a combination of a featureless continuum and spectral lines with a total brightness in the H-band that is a factor f_L brighter than the [Fe II] 1.64 μm line. Using the observed fluxes and the filter widths, the line contribution to the H band is $\sim 2f_L\%$, and even in the narrow [Fe II]-centered filter, is only $\sim 30\%$ due to the 1.64 μm line. Spectroscopically, the 1.64 μm line is the dominant line in the H band as found in observations by Gerardy & Fesen (2001) from FMK positions. While the 1.64 μm line is dominant ($f_L \simeq 1$) from FMK positions, the QSF have a wide range of lines, with $f_L \sim 2$. Thus the H band is dominated by continuum emission, with lines contributing less than 4% of the in-band flux. In the K_s band, the conclusion is even more clear, because of the

paucity of spectral lines. For most positions, there are no spectral lines detected in the K_s band (in our CorMASS data and the FMK positions from Gerardy and Fesen [2001]). Even using the line-rich QSF spectra, the total line brightness in the K_s band is 10% of the total line brightness in the H band, and spectral lines would contribute $< 1\%$ of the K_s -band flux. The conclusion that continuum dominates the wide bands is robust, and even after accounting for the uncertainties from star-subtraction methods, the line contribution would be less than 8% in the H bands, and less than 2% in K_s band.

Measuring the J band flux was challenging, because 2MASS barely detected the diffuse emission from the remnant. The 2MASS J band flux is 0.12 Jy, and the extinction-corrected flux is 0.39 Jy using A_v of 4.5 mag, which may be highly uncertain. Gerardy & Fesen (2001) show a higher resolution J band image, which is similar to our [Fe II] band image. Their J band spectra show a number of bright lines such as [Fe II], [S II] and [P II] such that the total flux of lines in the J band is 7-9 times greater than in H-band. Using the line fraction derived above for the H-band, we estimate that that lines contribute $\sim 20 - 40\%$ of the J-band flux. The reason the J-band and the narrow Fe-band images are similar is that they contain similar fractions of line emission.

3.2. Possible dust contribution to Cas A flux

The mid-infrared spectrum of Cas A revealed dust newly formed from the ejecta material, as well as gas lines (Douvion, Lagage & Pantin 2001; DLP01). A model for the mid-infrared spectrum using dust composed of pyroxene, quartz, and aluminum oxide, with cold (90 K) and warm (350 K) components can reasonably approximate the spectrum longward of $8 \mu\text{m}$ (DLP01). We estimated the dust contribution to the near-infrared brightness by calculating the ratio of the $2.2 \mu\text{m}$ to $8 \mu\text{m}$ brightness of small pyroxene (Dorschner et al. 1995) particles at 350 K, then scaling to the observed $8 \mu\text{m}$ brightness (DLP01). In Figure 3 of DLP01 it is evident that dust dominates at $8 \mu\text{m}$ and above, and the synchrotron component only begins to contribute significantly at $6 \mu\text{m}$. We find that the synchrotron emission is 3-4 orders of magnitude higher than the extrapolated dust model at $2.2 \mu\text{m}$. We also estimated the brightness of starlight scattered by the Cas A dust, using the interstellar radiation field (Mathis, Mezger, and Panagia 1983), an albedo of 0.6, and the same optical depth as inferred from the mid-infrared thermal emission model (mostly from the colder component). The scattering contribution is 4-5 orders of magnitude smaller than that of synchrotron emission. Therefore, at $2.2 \mu\text{m}$, synchrotron emission dominates over dust emission and scattering. Recent submillimeter observations of Cas A show no dust is present at $850 \mu\text{m}$ (Loinard 2002), which strengthens our conclusion of no dust contribution at $2 \mu\text{m}$.

4. Near-Infrared Synchrotron Radiation from Cas A

We show the broad-band spectrum of Cas A, from radio to TeV energies, in Figure 4. The data from Baars et al. (1977) for 10–35 MHz, Liszt & Lucas (1999) for 86 and 140 GHz, and Mezger et al. (1986) for 1.2mm data, are marked. The high energy data of RXTE (Allen et al. 1997), OSSE (The et al. 1996), EGRET (Esposito et al. 1996), and Whipple (Lessard et al. 1995) are also indicated. Our near-infrared points are above the fit to the radio data (solid line) with $\alpha = -0.77$ (where $\log S = \beta + \alpha \log \nu$, $\beta = 5.745 \pm 0.025$ for ν in MHz [Baars et al. 1977], which is equivalent to $\beta = 10.365$ for ν in Hz). This shows that the K_s flux before correcting for extinction is comparable to the lower-frequency extrapolation, and the extinction-corrected K_s flux is $\sim 70\%$ higher than that extrapolation. When we performed a weighted fit to the radio, mm and near-IR data, we obtain an index that is not significantly different from -0.77 and the value of the constant β is slightly higher than that in Baars et al. (10.409 ± 0.029 , see thick solid line in Fig. 4). The extrapolation of this spectrum fell below the near-IR data points, suggesting positive (concave-up) curvature. A flatter index than -0.77 has been suggested by Mezger et al. (1986); they found -0.65 . When we fit the 86 and 140 GHz, 1.2mm and $2\mu\text{m}$ data alone, $\alpha = -0.709 \pm 0.040$ and $\beta = 9.762 \pm 0.444$, showing a hardening to higher frequencies, although we cannot completely rule out the possibility that the excess near-IR flux above the extrapolation is due to contamination from line emission.

It is possible that the concave spectrum between 140 GHz and near-IR is at least partially due to spectral-index variations across the remnant. If different shocks produce slightly different spectral indices, perhaps because of differences in Mach number, shocks with harder spectra will come to dominate at higher frequencies, and the spatially integrated spectrum will be concave. Spectral-index variations between 1.4 and 5 GHz were studied by Anderson et al. (1991), who obtained values from -0.64 to -0.92 . Figure 5 is a two-color image with the radio image (1.4 GHz; Anderson et al. 1991) in red and the star-subtracted K_s -band image in green, and shows spectral-index variations. Radio-dominated regions (red in Figure 5) have a steeper spectral index, and K_s -band dominated regions (green in Figure 5) have a flatter spectral index between the radio and K_s frequencies. The noticeable steep spectral-index regions (red in Figure 5) are the southeastern shell and knots, and a blob in the west outside of the shell (at RA of $23^{\text{h}} 23^{\text{m}} 8.5^{\text{s}}$, $\delta = 58^{\circ} 48' 44''$). By contrast, the southwest rim appears to have a relatively flat spectrum. This image is indeed very similar to the radio spectral-index map between 1.4 and 5 GHz, which is shown in Figure 3 of Anderson et al. (1991). Figure 6 shows K_s -band and radio radial profiles averaged over $5^{\circ} - -10^{\circ}$ sectors toward the north, northeast, southeast, and southwest directions (each position angle is given in the Figure caption). While the K_s band and radio profiles are similar in the N and NE (except the radio is more sharply peaked in the shell), the K_s image is noticeably fainter in the SE shell and brighter in the SW shell, which is consistent with what we see in Figure 5.

We have also constructed images using the ‘spectral tomography’ technique (Katz-Stone & Rudnick 1997), in which scaled versions of one image are subtracted from another. That is, for a series of trial values $\alpha_t (< 0)$, we subtract from the radio image the K_s -band image mul-

multiplied by $(\nu_{\text{radio}}/\nu_{\text{IR}})^{\alpha_t}$. In such images, emission with a spectrum steeper than α_t appears positive, while flatter-spectrum emission appears negative. In Figure 7, we show images for $\alpha_t = -0.61, -0.67, -0.73$, and -0.77 . Since the -0.61 image is essentially all positive, and the -0.77 image all negative, the radio-near IR spectral index of different regions in Cas A is bracketed by these values. For $\alpha_t = -0.67$ and -0.73 we see both positive and negative structure. The disappearance of much of the emission along the bright southwestern and northern rims in the -0.67 image indicates that the average radio-near IR spectral index in these regions is about -0.67 . Similarly, the southeastern rim mostly vanishes in the -0.73 image shows that the average spectral index along the southeastern rim is about that value. These results are consistent with the two-color radio/ K_s image, in which the SE rim appears steeper, while most of the rest of the remnant is flatter. There is a great deal of other small-scale structure in these images whose more detailed investigation might provide useful information on the location and properties of electron acceleration.

However, it is not clear that the observed integrated-spectrum concavity can be produced by simply adding contributions from regions with straight spectra with different slopes. For instance, a region with a 1.4-5 GHz radio spectral index flatter than the average by 0.13 would be about 5 times brighter at K_s band than a region of comparable brightness at 1.4 GHz with the average spectrum. Such large variations do not appear to be the case. But another explanation for the concavity is available. Such concave-up curvature of the spectrum is predicted by nonlinear shock-acceleration models in which shock transitions are broadened by pre-acceleration from cosmic rays diffusing ahead of the shock, if particles' diffusion lengths increase with energy. In this case, more energetic particles feel a higher velocity jump between upstream and downstream fluids, and the spectrum is flatter at those energies (Eichler 1984; Ellison & Reynolds 1991). Hints of this effect are seen in Tycho's and Kepler's SNRs (Reynolds & Ellison 1992) as well as in Cas A. If such concavity can be shown to be true for localized regions as well as for the spatially integrated spectrum, it will strongly support the case for such nonlinear effects. Other theories of particle acceleration, such as stochastic (second-order Fermi) acceleration in magnetohydrodynamic turbulence, predict a steepening spectrum (e.g., Cowsik & Sarkar 1984), so that our observation supports diffusive (first-order Fermi) shock acceleration instead. A recent paper by Jones et al. (2003) also showed concavity of the spectrum from a small portion of the bright shell with the detection of polarized flux at $2.2\mu\text{m}$, which reinforces presence of concavity of the spectrum, i.e. presence of non-linear shocks in Cas A.

The synchrotron spectrum should eventually roll off due to one of several limitations on electron acceleration: radiative losses, finite acceleration time, or particle escape (Reynolds 1998; Sturmer et al. 1997; Baring et al. 1999). For any of these, the electron distribution is likely to cut off no faster than exponentially (Reynolds 1998) with an e-folding energy E_{max} . For a homogeneous source, the rolloff frequency is related to E_{max} by

$$\nu_{\text{rolloff}} = 4.7 \times 10^{15} \left(\frac{B_{\perp}}{\text{mG}} \right) \left(\frac{E_{\text{max}}}{\text{TeV}} \right)^2 \text{ Hz}$$

where B_{\perp} is the sky-plane component of the magnetic field. A lower limit for the roll-off frequency can be estimated directly from the high-frequency end of the K_s band, which is 1.5×10^{14} Hz. In a magnetic field B , synchrotron radiation at this frequency is produced by electrons with energies $E = 0.29 B_{\text{mG}}^{-1/2}$ erg or ~ 0.2 TeV, where B_{mG} is the mean magnetic field in milliGauss. These values assume that B lies entirely in the plane of the sky, since this gives us the most conservative lower limit on E . Our claim of the presence of electrons at these energies makes it plausible that some portion of the X-ray emission is synchrotron as well.

Reynolds & Keohane (1999) obtained an upper limit to the rolloff frequency of 3.2×10^{17} Hz, by assuming all the X-ray emission to be synchrotron. Since the X-ray emission obviously contains thermal emission with a rich line spectrum, this is a very conservative upper limit. Allen et al. (1997) used a cut-off frequency of 2.4×10^{17} Hz (1 keV). However, the cut-off frequency is very sensitive to the values of spectral index from the radio.

The half-life of electrons with Lorentz factor γ radiating in a magnetic field B is given by

$$t_{1/2} = \frac{5.1 \times 10^8}{\gamma B^2} \text{ s} = 1.81 \times 10^{16} \nu^{-1/2} B_{\text{mG}}^{-3/2} \text{ s}$$

where we have averaged over magnetic-field directions. The electrons radiating in the K_s band ($\nu = 1.5 \times 10^{14}$ Hz) have lifetimes of only about $47 B_{\text{mG}}^{-3/2}$ yr. With typical velocities in Cas A of several thousand km s^{-1} , electrons in such strong fields could travel distances of order tens of arcsec (for $d = 3.4$ kpc; Reed et al. 1995) in a loss time. The synchrotron emissivity varies roughly as $n_{\text{els}} B^{1+\alpha}$, where n_{els} is the energy density in relativistic electrons and α is the spectral index. If the magnetic field evolves by flux freezing and the relativistic electrons at these energies have relatively short diffusion lengths, we have n_{els} is proportional to n , the thermal gas density, and B proportional to a power of n between 0 and 1.8. Then the synchrotron emissivity varies as roughly n^2 , like the optical emissivity; both optical emission and synchrotron emission would be prominent in high density regions, showing the morphological difference between the radio and optical is not due to density difference. The smoothness of the K_s band and radio images, relative to optical images that more directly trace the shock fronts and high thermal-gas densities, is due to the relatively large diffusion distances of the extremely high-energy synchrotron emitting electrons, resulting in a generally smoother distribution of those electrons than that of thermal gas.

Even though the synchrotron loss time for the K_s -band-emitting electrons is substantially less than the age of Cas A, it is much longer than the time required for shock acceleration to produce the electrons. We can estimate the acceleration time based on the general expression in Forman & Morfill (1979), for the particular case of electron mean free path proportional to gyroradius, $\lambda_{\text{mfp}} = \eta r_g$ with $r_g = E/eB$ for extreme-relativistic electrons, and making other reasonable assumptions detailed in Reynolds (1998). The acceleration time for parallel shocks (shock normal parallel to the upstream magnetic field) is

$$\tau_{\text{acc}} = 1.3 \eta (B_{\text{mG}})^{-1} u_8^{-2} E \text{ yr}$$

where u_8 is the shock speed in units of 10^8 cm s⁻¹, and E is in erg. For perpendicular shocks, in which we assume a compression ratio of 4, the acceleration time is

$$\tau_{\text{acc}} = 0.53 \eta^{-1} (B_{\text{mG}})^{-1} u_8^{-2} E \text{ yr.}$$

We infer that shocks can produce the K_s -band emitting electrons in times of order one year. This very short timescale suggests that variability in acceleration, if not depletion, of these electrons could be observed over timescales of the same order. Now the radio morphology of Cas A makes it clear that there is no single acceleration site like the outer shock wave in SN 1006; instead, particle acceleration appears to take place in many small knots all over the remnant (Anderson et al. 1991). This picture can be supported by detailed theoretical analysis (Atoyan et al. 2000). In their model, the magnetic field in the knots where acceleration takes place is much larger than that in the general remnant volume, so one would expect longer synchrotron lifetimes once electrons diffused out of the acceleration zones. In any case, to the extent that our K_s band image resembles the radio, synchrotron losses are evidently not dominant, or we would expect to see less diffuse emission and a greater concentration in knots. But small differences between the images of Figure 5 shows that it is not impossible that this greater concentration has already begun to occur.

While most authors agree that shock acceleration produces the relativistic electrons in Cas A, it is not impossible that some form of turbulent or stochastic acceleration is responsible (e.g., Cowsik & Sarkar 1984). One must ask if this mechanism, designed to describe radio emission, can in the time available produce the ~ 1 erg electrons required by our near-infrared image. Melrose (1974) gives expressions for acceleration rates in magnetohydrodynamic turbulence which show that once electrons are substantially suprathermal (‘injected;’ a necessity for shock acceleration as well), they can reach relativistic energies in a fraction of a year. Subsequent acceleration of relativistic electrons in MHD turbulence with amplitude $\delta B/B \equiv \epsilon$ takes place on a timescale

$$\tau_{\text{acc}} \sim \frac{1}{\epsilon^2} \frac{r_g}{c} \left(\frac{v_A}{c} \right)^{-2}$$

where v_A is the Alfvén speed and r_g is the electron’s gyroradius. Strictly speaking, this result is true in the quasilinear approximation ($\epsilon \ll 1$), but it should provide at least a rough estimate for $\epsilon = 1$ to give us a conservative idea of the fastest possible acceleration. In the above expression, ϵ refers to the amplitude of waves resonant with the particular particle, which must be presumed to exist (perhaps generated by the particles themselves). Again assuming that the electron mean free path is a multiple of its gyroradius, $\lambda_{\text{mfp}} \equiv \eta r_g$, quasilinear theory then gives $\eta = (\delta B/B)^{-2} = \epsilon^{-2}$, so we can rewrite the acceleration time as $\tau_{\text{acc}} \sim (\lambda_{\text{mfp}}/c)(v_A/c)^{-2}$. Since in the extreme-relativistic limit, $r_g = E/eB$, with E the particle energy, the acceleration time to a particular energy is just proportional to that energy. For the strong fields we anticipate in Cas A, $v_A = 2.2 \times 10^8 B_{\text{mG}}(\mu n_H)^{-1/2}$ cm s⁻¹, where the matter density is $\rho = \mu m_p n_H$. So $v_A/c \sim 10^{-2}$, and with $r_g = 2 \times 10^{12} E B_{\text{mG}}^{-1}$ cm, we estimate $\tau_{\text{acc}} \sim 10^6$ s to reach energies adequate to produce infrared synchrotron radiation (in these strong fields) – comparable to the rate of shock acceleration. This can occur because the strong magnetic fields in Cas A can give Alfvén speeds comparable to

the current, decelerated outer blast-wave speed. So stochastic acceleration can certainly proceed rapidly enough to explain our observations. The spectrum produced by stochastic acceleration will depend on the properties of the turbulence and it is not clear if the required remarkably flat, slightly hardening spectrum can in fact be produced. However, neither shock acceleration nor stochastic acceleration can be ruled out on the basis of acceleration-time arguments.

5. Summary and conclusions

The 2MASS near-infrared images reveal emission from Cas A in the J, H, and K_s bands. The images reveal a shell-like morphology shown in Figure 1. The K_s and H band images are brighter than the J band image. The three-color image demonstrates the difference: K_s emission is dominant for the majority of Cas A, and H band emission is noticeable in the southwestern shell. Near-infrared spectra showed [Fe II] lines in J ($1.25\mu\text{m}$) and H ($1.64\mu\text{m}$), and no lines were detected within the K_s band.

A high-resolution Palomar PFIRCAM narrow-band image of [Fe II] ($1.64\mu\text{m}$) (see Figure 2) is similar to the optical image of Cas A, showing sharp filamentary and knotty structures of Fe-rich ejecta. The PFIRCAM K_s band image is much smoother and more diffuse than the ejecta structure that dominates the optical images (and is present in the [Fe II] image). Instead, the K_s image is remarkably similar to the radio image of Cas A, suggesting that the physical mechanism that produces radio emission—synchrotron radiation—is also responsible for the K_s band emission. We measure a total flux of Cas A in the K_s band of 0.32 ± 0.03 Jy, implying a flux of $0.53^{+0.12}_{-0.04}$ Jy after correcting for extinction. The spectral energy distribution of Cas A shows that the near-infrared flux is close to an extrapolation of the radio fluxes, supporting our interpretation of the near-IR flux as synchrotron radiation. The near-infrared K_s band fluxes are actually a few tens of percent higher than an extrapolation of the radio fluxes. Such positive (concave-up) curvature of the spectrum (hardening to higher frequencies) is predicted by nonlinear shock-acceleration models in which shock transitions are broadened by pre-acceleration from cosmic rays diffusing ahead of the shock, if particles' diffusion lengths increase with energy.

The synchrotron spectrum may roll off due to any of several possible limitations on electron acceleration including radiative losses, acceleration time, or particle escape; this is measured as the rolloff frequency. Our near-infrared emission measurement gives us a lower limit to the roll-off frequency of 1.5×10^{14} Hz. Synchrotron radiation at this frequency is produced by electrons with energies $E = 0.3B_{\text{mG}}^{-1/2}$ erg or about 0.2 TeV, where B_{mG} is the mean magnetic field in milliGauss. The synchrotron loss time for electrons radiating in the K_s band is only about $47 B_{\text{mG}}^{-3/2}$ yr. The fact that such electrons can thus travel only distances on the order of tens of arcsec implies particle acceleration takes place in many sites all over the remnant. Our K_s band image resembles the radio, so synchrotron losses evidently do not dominate the small-scale structure. The acceleration time scale for electrons with energy high enough to produce the near-infrared emission from Cas A

is of order a year (or less), so either shock or stochastic acceleration is rapid enough to accelerate electrons to the required energies.

Our results confirm that supernova remnants are high-energy cosmic-ray acceleration sites that can produce 0.2 TeV particles. We also show that near-infrared observations are a good tool to study synchrotron radiation and cosmic-ray acceleration in supernova remnants.

J. Rho thanks Pierre-Olivier Lagage for discussion on synchrotron emission from mid-infrared observation, which gave her strong motivation for this project.

REFERENCES

- Allen, G.E., Keohane, J.W., Gotthelf, E.V., Petre, R., & Johoda, K., 1997, *ApJL*, 487, L97
- Anderson, M. A., & Rudnick, L., Leppik, P., Perley, R., & Braun, R., 1991, 373, 157
- Aharonian et al. 2001, *A &A*, 370, 112
- Asvarov, A.I., Guseinov, O.Kh., Dogel, V.A., & Kasumov, F.K. 1989, *Sov.Astron.* 33, 532
- Atoyan, A.M., Tuffs, R.J., Aharonian, F.A., & Völk, H.J. 2000, *A&A*, 354, 915
- Baars, J.W.M., Genzel, R., Pauliny-Toth, I.I.K., & Witzel, A., 1977, *A&*, 61, 99
- Baring, M.G., Ellison, D.C., Reynolds, S.P, Grenier, I.A., & Goret, P., 1999, 513, 311
- Bleeker, J.A.M., Willingale, R., van der Heyden, K., Donnerl, K., Kaastra, J.S., Aschenbach, B., & Vink, J. 2001, *A&A*, 365, L225
- Borkowski, K. J., Rho, J., Reynolds, S. P., & Dyer, K. K. 2001, *ApJ*, 550, 334
- Cowsik, R., & Sarkar, S. 1984, *MNRAS*, 207, 745 (erratum, 1984, *MNRAS*, 209, 719)
- Dorschner, J., Begemann, B., Henning, T., Jäger, C., & Mutschke, H. 1995, *A&A*, 300, 503–520
- Douvion, T., Lagage, P.O. & Pantin, E., 2001, *A&A*, 369, 589 (DLP01)
- Dyer, K.K., Reynolds, S.P., Borkowski, K.J., Allen, G.A., & Petre, R. 2001, *ApJ*, 550, 334
- Eichler, D. 1984, *ApJ*, 277, 429
- Ellison, D.C., Goret, P., Baring, M.G., Grenier, I.A., & Lagage, P.-O. 1999, *Proc. 26th Int. Cosmic Ray Conf. (Salt Lake City)*, 3, 468
- Ellison, D.C., & Reynolds, S.P. 1991, *ApJ*, 378, 214
- Esposito, J.A., Hunger, S.D., Kanbach, G., & Sreekumar, P., 1996, *ApJ*, 461, 820

- Fesen, R.A., Becker, R.H., & Blair W.T., 1987, ApJ, 313, 378
- Gerardy, C. L., & Fesen, R. A., 2001, ApJ, 121, 2781
- Gotthelf, E.V., Koralesky, B., Rudnick, L., Jones, T.W., Hwang, U., & Petre, R. 2001, ApJ, 552, L39
- Hendrick, S.P., & Reynolds, S.P. 2001, ApJ, 559, 903
- Hurford, A. P. & Fesen, R. A., 1996, ApJ, 469, 246
- Jones, T.J., Rudnick, L., Delaney, T., & Bowden, J., 2003, ApJ, in press (also see astro-ph/0212544)
- Katz-Stone, D.M., & Rudnick, L. 1997, ApJ, 488, 146
- Koyama, K., et al. 1995, 47, 711
- Koyama, K., et al. 1997, PASJ, 49, L7
- Laming, J.M. 2001, ApJ, 546, 1149
- Lessard, R.W., et al. 1995, in Proc. 24th Int. Cosmic-Ray conf. (Rome), 2, 475
- Loinard, L., 2002, “Winds, Bubbles and Explosions” Patzcuaro in Mexico, in press
- Liszt, H., & Lucas, R., 1999, A&A, 347, 258
- Mathis, J.S., Mezger, P.G., & Panagia, N. (1983), A&A, 128, 212
- Melrose, D. B., 1974, SoPh, 37, 353
- Mezger, P.G., Tuffs, R.J., Chini, R., Kreysa, E., & Gemünd, 1986, A&A, 167, 145
- Reach, W. T., Rho, J., Jarrett, T. H., & Lagage, P.-O. 2002, ApJ, 564, 302
- Reed, J.E., Hester, J.J., Fabian, A.C., & Winkler, P.F., 1995, ApJ, 440, 706
- Reynolds, S. P., 1998, ApJ, 493, 375
- Reynolds, S.P., & Ellison, D.C. 1992, ApJ, 399, L75
- Reynolds, S.P., & Keohane, J.W. 1999, ApJ, 525, 368
- Rho, J., Jarrett, T.H., Cutri, R.M., & Reach, W.T., 2001, ApJ, 547, 885
- Rho, J., Dyer, K.K., Borkowski, K.J., & Reynolds, S.P., 2002, ApJ, 581, 1116
- Rieke, G. H., & Lebofsky, M.J., 1985, ApJ, 288, 618
- Searle, L., 1971, ApJ, 168, 41

- Skrutskie, et al., 1997, “The impact of large scale near-IR sky surveys”, ed.by F. Garzon et al., p25
- Slane, P. , Gaensler, B. M., Dame, T. M., Hughes, J. P., Plucinsky, P. P. & Green, A. 1999, ApJ, 525, 357
- Slane, P., Hughes, J.P., Edgar, R.J., Plucinsky, P.P., Miyata, E., H. Tsunemi, & B. Aschenbach., 2001, ApJ, 548, 814
- Sturmer, S.J., Skibo, J. G., Dermer, C. D., & Mattox, J.R., 1997, ApJ, 490, 619
- Tanimori, T., et al. 1998, ApJ, 497, L25
- The, L.-S., Leising, M.D., Kurfess, J.D., Johnson, W.N., Hartmann, D.H., Gehrels, N., Grove, J.E., & Purcell, W.R. 1996, A&AS, 120, 357
- Tuffs, R.J., Drury, L., Fischera, J., et al. 1997, Proc. 1st ISO Workshop on Analytical Spectroscopy (ESA SP-419), p. 177
- Wilson, J. C. et al. 2001, PASP, 113, 227

Fig. 1.— Mosaiced 2MASS three color Atlas Image of Cas A. The color ranges are 0.7-3.7 μJy (J in blue), 5-29 μJy (H in green), and 7-38 μJy (K_s in red) per 1'' pixel. Most of the diffuse emission is K_s band (red) dominated, but there are a few places showing significant H band (green) emission, in particular, in the southwestern shell. The position of the center is ($23^{\text{h}} 23^{\text{m}} 25.7^{\text{s}}$, $58^{\circ} 48'52''$ in J2000), and the image size is 12'.

Fig. 2.— Mosaiced Palomar PFRICAM two-color images of K_s (red) and [Fe II] (blue). The narrow-band [Fe II] image shows filamentary and knotty structures (from ejecta material) that are not present in the broad-band K_s image, which is dominated by synchrotron emission. The colors are 5-82 μJy (blue) and 2-11 μJy (red) per 0.5'' pixel. The center of the image is the same as Fig. 1 and the image size is 6.4'.

Fig. 3.— (a) The K_s band image of Cas A. (b) Radio image of Cas A at 1.4 GHz (Anderson et al. 1991). The K_s and radio images are remarkably similar, except of course for the presence of unrelated stars in the K_s image.

Fig. 4.— Broad band frequency and flux spectrum of Cas A. The near-infrared K_s flux is marked with an asterisk and the extinction corrected flux is marked as a square (assuming $A_v=4.5$ mag). The solid line has a spectral index of -0.77 , which is derived using all the radio, near-IR, 86 GHz, and 140 GHz fluxes, with an exponential cut-off applied. The dash-dotted line has a spectral index of -0.71 , which is derived using only the near-IR, 86 GHz, and 140 GHz fluxes. The dash-two-dotted lines are nonthermal-bremsstrahlung (NB), inverse Compton scattering of the cosmic microwave background (IC), and the decay of neutral pions (π^0) from Allen et al. (1997).

Fig. 5.— Two color images of K_s band (green) and radio (red). Stars have been subtracted from the K_s band image. The area emitting in both the K_s band and radio appears in yellow. The three saturated stars are masked. This image highlights differences between the K_s and radio emission from the remnant, with the southeast being relatively radio-bright.

Fig. 6.— Radial profiles of K_s band (solid) and radio (dashed) images. We chose the center position of RA = $23^{\text{h}} 23^{\text{m}} 26^{\text{s}}$, Dec = $58^{\circ}48'42''$ (J2000); N, covering position angles (eastward from the north) of $355\text{-}360^{\circ}$; NE, covering P.A. of $45\text{-}50^{\circ}$; SE, covering P.A. of $135\text{-}145^{\circ}$; SW, covering P.A. of $210\text{-}220^{\circ}$. The relative fluxes are conserved within each of K_s and radio images.

Fig. 7.— ‘Spectral tomography’ maps: from the radio image we subtract the K_s -band image multiplied by $(\nu_{\text{radio}}/\nu_{\text{IR}})^{\alpha_t}$. White corresponds to positive values, softer (steeper) than the trial index, and dark to negative values, harder than the trial index. The scale is between -0.03 to 0.03. The three saturated stars are masked shown in white. (a: top left) $\alpha_t = -0.61$: the spectral index is steeper than -0.61 for all of Cas A. (b: top right) $\alpha_t = -0.67$: SW shell turns positive to negative. (c: bottom left) $\alpha_t = -0.73$: northern shell and outer shock of northern shell change to negative. (d: bottom right) $\alpha_t = -0.77$: the only positive structure is the western edge knot. We deduce that the approximate spectral index is ~ -0.67 for SW shell, ~ -0.73 for the northern shell and the upper part of SE shell, ~ -0.77 for the lower part of SE shell, and steeper than ~ -0.77 for the western edge knot.

This figure "f1color.jpg" is available in "jpg" format from:

<http://arxiv.org/ps/astro-ph/0303215v1>

This figure "f2color.jpg" is available in "jpg" format from:

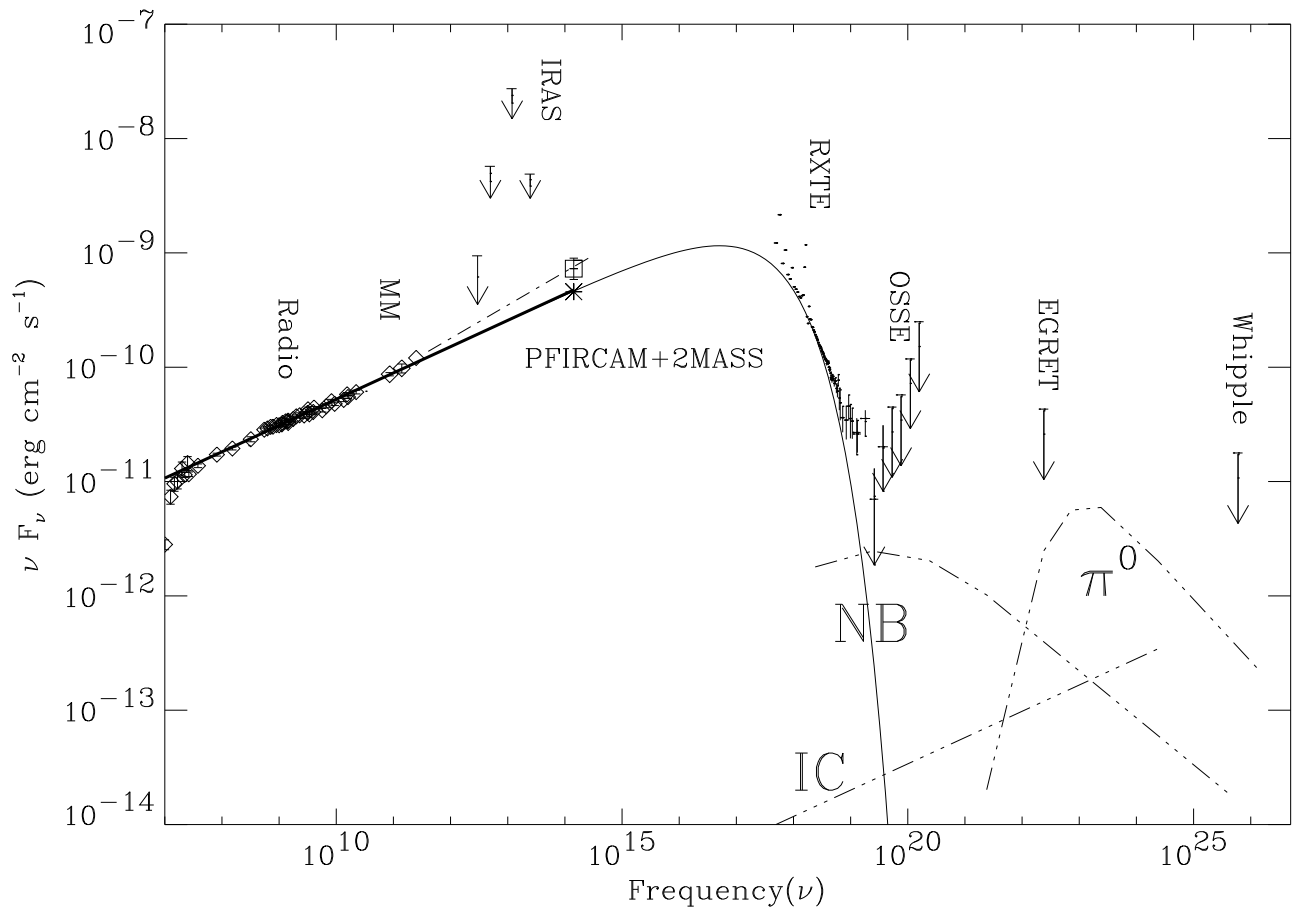
<http://arxiv.org/ps/astro-ph/0303215v1>

This figure "f3a.jpg" is available in "jpg" format from:

<http://arxiv.org/ps/astro-ph/0303215v1>

This figure "f3b.jpg" is available in "jpg" format from:

<http://arxiv.org/ps/astro-ph/0303215v1>



This figure "f5color.jpg" is available in "jpg" format from:

<http://arxiv.org/ps/astro-ph/0303215v1>

